Draft version March 2, 2018
Typeset using LaTeX twocolumn style in AASTeX62

Regions paper

T. Whitbread,[1] A. R. Yeates,[1] and A. Muñoz-Jaramillo[2]

[1] Department of Mathematical Sciences, Durham University, Durham, DH1 3LE, UK
[2] Southwest Research Institute, 1050 Walnut St. #300, Boulder, CO 80302, USA

(Received; Revised; Accepted)

ABSTRACT

We test recent claims that the polar field at the end of Cycle 23 was weakened by a small number of large, abnormally oriented regions, and investigate what this means for solar cycle prediction. We isolate the contribution of individual regions from magnetograms for Cycles 21, 22 and 23 using a 2D surface flux transport model, and examine the relationship between a region's axial dipole moment contribution and its emergence latitude, flux, and initial axial dipole moment. We find, in agreement with other authors, that emergence latitude primarily determines the contribution of a region to the end-of-cycle axial dipole moment, with flux and initial axial dipole moment playing secondary, but nevertheless important, roles. Although the top ∼10% of contributors tend to define sudden large variations in the axial dipole moment, the cumulative contribution of many weaker regions can not be ignored. In order to recreate the axial dipole moment to a reasonable degree, many more regions are required in Cycle 23 than in Cycles 21 and 22 when ordered by contribution. We suggest that the negative contribution of the most significant regions of Cycle 23 could indeed be a cause of the weak polar field at the following cycle minimum and the low-amplitude Cycle 24.

Keywords: magnetohydrodynamics (MHD) — Sun: activity— Sun: photosphere — Sun: sunspots

1. INTRODUCTION

There is a strong correlation between the strength of the Sun's polar magnetic field at solar cycle minimum and the strength of the following cycle (e.g., Schatten et al. 1978; Muñoz-Jaramillo et al. 2013). This relationship calls for accurate predictions of the polar field. Common methods for simulating the evolution of the radial magnetic field at the surface include using dynamo models (for a review, see Charbonneau 2014), but surface flux transport (SFT) models (Wang et al. 1989; Baumann et al. 2004; Sheeley 2005; Jiang et al. 2010; Mackay & Yeates 2012; Upton & Hathaway 2014; Hathaway & Upton 2016), introduced in the 1960s (Babcock 1961; Leighton 1964), have risen in popularity over the last decade due to their relative simplicity and accuracy.

Surface flux transport models describe the evolution of magnetic regions on the solar surface, which appear due to the rise of buoyant flux tubes (Fan 2009). Generally they emerge with a leading polarity and an opposing trailing polarity with respect to the east-west direction, and so are known as bipolar magnetic regions (BMRs). There is hemispheric asymmetry in the leading polarities, which are generally the same across a hemisphere, according to Hale's polarity law (Hale 1924). Helical convective motions in the solar interior impart a tilt to each BMR with respect to the east-west line (the line that connects the centres of the opposing polarities), with the leading polarity located closer to the equator. The effect is stronger at higher latitudes according to Joy's law (Howard 1991), and a sinusoidal fit for the relationship between tilt angle α and latitude λ is $\alpha = 32.1 \sin\lambda$ (Stenflo & Kosovichev 2012), although it should be noted that there is significant variation between different regions. These deviations from Joy's Law could be the key characteristics in determining polar field strength at cycle minimum, as discussed below.

After emergence, the magnetic flux then diffuses across the surface by being pushed to the edges of convection cells (Leighton 1964). This can lead to cross-equatorial flux cancellation between the leading polarities from opposite hemispheres, and any remaining

Corresponding author: T. Whitbread
tim.j.whitbread@durham.ac.uk

trailing flux is transported poleward by a combination of diffusion and a meridional flow (Howard 1979) of the order $\sim$10–20 $\mathrm{m\,s^{-1}}$ (e.g. Komm et al. 1993; Jackiewicz et al. 2015). It is this built-up polar field which provides an early insight into the amplitude of the following cycle.

Of particular interest is the unusually weak polar field (and equivalently weak axial dipole moment) at the end of Cycle 23 (Muñoz-Jaramillo et al. 2012), which in turn is believed to be responsible for the low amplitude of Cycle 24. Jiang et al. (2015) used the BMR data of Li & Ulrich (2012) to investigate the effect of tilt angle on axial dipole moment contribution D, using an empirical relation involving tilt angle, latitude and area (Jiang et al. 2014):

$$D \propto A^{\frac{3}{2}} \sin\alpha \exp\left(-\frac{\lambda^2}{110}\right), \tag{1.1}$$

where A is the area, α is the tilt angle, and λ is the emergence latitude of each region. They found that axial dipole moment contributions from observed tilt angles in Cycle 23 follow those obtained by assuming Joy's Law at latitudes above $\pm 10°$. Nearer the equator, the regions with observed tilt angles contribute substantially less than would be expected from Joy's Law, contrary to the behaviour of Cycles 21 and 22, which follow the Joy's Law contributions more closely at all latitudes. This led to the suggestion that a single large anti-Hale or anti-Joy region emerging at a low latitude, or across the equator (Cameron et al. 2013, 2014), has the ability to significantly alter the dipole moment, and this could have been the catalyst behind the weak polar field at the end of Cycle 23. Therefore the stochasticity behind the properties of emerging regions provides a problem for those attempting to predict the amplitude of future cycles, especially given that the magnetic flux in a large active region is similar to the total polar flux (Wang & Sheeley 1991). With this in mind, it may not be possible to make reliable predictions until the end of the cycle, unless random fluctuations of active region properties are taken into account. Indeed, Nagy et al. (2017) recently demonstrated in a 2×2D dynamo model that large 'rogue' regions can drastically affect the evolution of future solar cycles and introduce hemispheric asymmetries. Such large regions emerging during the early phases of a cycle can even affect the amplitude and duration of the same cycle. In this particular dynamo model, the effect of a single region can persist for multiple cycles. Nagy et al. (2017) found that the effect of a region in their model is dependent on its axial dipole moment at time of emergence, which is in turn approximated by Equation 1.1. So bipolar regions near the equator, and/or with large tilt angle, are are particularly strong contributors, although significant effects were found for regions even up to $\pm 20°$ latitude.

In this paper we investigate these claims further by simulating the evolution of real active regions from Cycles 21, 22 and 23 using a 2D SFT model[a] with an automated region identification and assimilation process (Yeates et al. 2015). This allows us to identify particular observed properties which could have defined the contribution of each region to the axial dipole moment. In this paper, the emerging regions are determined from NSO line-of-sight magnetograms. In Section 2 we analyse said properties of regions. In Section 3 we discuss the implications of our findings for future cycle predictions, before concluding in Section 4.

2. CONTRIBUTIONS OF INDIVIDUAL REGIONS TO THE AXIAL DIPOLE MOMENT

We investigate the distribution of various magnetic region properties, namely latitude, magnetic flux, and initial and final axial dipole moment. The regions and their properties are extracted from NSO Kitt Peak and SOLIS synoptic magnetograms[b], and the overall photospheric evolution is simulated using the 2D SFT model described in Yeates et al. (2015). The 2D model is fully automated and is constructed such that new regions replace pre-existing ones, rather than being superimposed on them. This ensures that the magnetic field, and consequently the axial dipole moment, is updated correctly throughout the simulation. The radial component of the magnetic field in 2D, $B\,(\theta, \phi, t)$, evolves according to:

$$\begin{aligned}\frac{\partial B}{\partial t} =& -\omega\,(\theta)\,\frac{\partial B}{\partial \phi} - \frac{1}{R_\odot \sin\theta}\frac{\partial}{\partial\theta}\Big(v\,(\theta)\sin\theta\, B\Big) \\ &+ \frac{\eta}{R_\odot^2}\left[\frac{1}{\sin\theta}\frac{\partial}{\partial\theta}\left(\sin\theta\frac{\partial B}{\partial\theta}\right) + \frac{1}{\sin^2\theta}\frac{\partial^2 B}{\partial\phi^2}\right] \\ &- \frac{1}{\tau}B + S(\theta,\phi,t),\end{aligned} \tag{2.1}$$

where $R_\odot$ is solar radius, $\omega\,(\theta)$ represents differential rotation, η is turbulent diffusivity, representing the diffusive effect of granular convective motions, τ is an exponential decay term added by Schrijver et al. (2002) to improve regular polar field reversal, and $S(\theta, \phi, t)$ is a source term for newly emerging magnetic regions. The profile $v\,(\theta)$ describes poleward meridional flow, which we define using the following functional form:

$$v\,(\theta) = -v_0 \sin^p\theta \cos\theta, \tag{2.2}$$

[a] https://github.com/antyeates1983/sft_data

[b] http://solis.nso.edu/0/vsm/vsm_maps.php

where p determines the latitude of peak velocity and low-latitude gradient. In order to define the initial conditions, we use the profile of Svalgaard et al. (1978):

$$B(\theta, 0) = B_0 |\cos\theta|^7 \cos\theta, \tag{2.3}$$

where B_0 is the initial field strength. The 2D model also contains a parameter B_{par} which acts as a threshold: only regions with magnetic flux above this value are assimilated into the simulation. All simulations are performed using the optimal values for diffusivity, meridional flow, initial field strength, exponential decay and assimilation threshold, obtained by Whitbread et al. (2017) using the genetic algorithm PIKAIA[c,d] (Charbonneau & Knapp 1995; Metcalfe & Charbonneau 2003). These optimum values are shown in Table 1, with associated 'acceptable ranges' below each entry. Note that we keep these parameters fixed across the three cycles, and that B_0 is the initial field strength at the start of Cycle 21; each other cycle immediately follows on from the final state of the preceding cycle. We use the optimal value of $B_{\mathrm{par}} = 39.8\,\mathrm{G}$ found in Whitbread et al. (2017). 'Optimal' in this sense refers to the ability to best match the simulated and observed butterfly diagrams, and the optimal butterfly diagram for Cycles 21 to 23 is shown in the top panel of Figure 1. The bottom panel shows the observed butterfly diagram obtained from full-disk images from US National Solar Observatory, Kitt Peak, which underwent a polar field correction procedure described by Petrie (2012). It should be stressed that all conclusions made in this paper are with respect to these optimal parameter values. For differential rotation, the parametrization of Snodgrass & Ulrich (1990) is used:

$$\omega(\theta) = 0.521 - 2.396\cos^2\theta - 1.787\cos^4\theta\,\mathrm{deg\,day}^{-1}. \tag{2.4}$$

We also include an exponential decay term of the form $-\frac{1}{\tau}B$. Baumann et al. (2006) offered a physical explanation for the extra term: it is the effect of inward radial diffusion of flux into the convection zone, which is not directly accounted for in the SFT model. Although it was not originally included in this particular 2D model (Yeates et al. 2015), and Whitbread et al. (2017) showed that it is not necessary in this model for replicating the evolution of the dipole moment for an *individual* cycle, we use it here to ensure regular polar field reversal over multiple cycles and to justify comparison with Nagy et al. (2017), who also utilized such a term. Later we present the case without decay and show that similar conclusions hold in both regimes.

[c] http://www.hao.ucar.edu/modeling/pikaia/pikaia.php
[d] http://www.hao.ucar.edu/Public/about/Staff/travis/mpikaia/

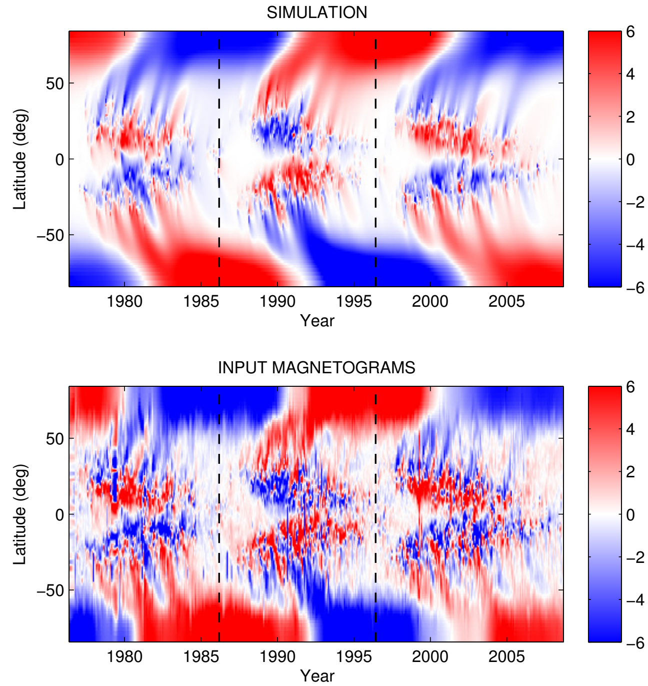

Figure 1. Top: Optimal butterfly diagram for Cycle 21 through to Cycle 23, simulated using the parameters from Table 1. Bottom: 'Ground truth' data for the same period. Vertical dashed lines indicate start/end points of cycles as used in this paper.

The axial dipole moment of region i is given by:

$$D_i(t) = \frac{3}{2}\int_0^{\pi}\int_0^{2\pi} B_i(\theta, \phi, t)\cos\theta\sin\theta\, d\phi\, d\theta. \tag{2.5}$$

To aid visualization we will also use the relative axial dipole moment D_{rel}, which is defined as a region's axial dipole moment divided by the change in total axial dipole moment over the whole cycle, in the simulation with all regions included:

$$D_{\mathrm{rel}}(t) = \frac{D_i(t)}{D_{\mathrm{tot}}(T)}, \tag{2.6}$$

where T is the time of the end of the cycle. The simulation is repeated and D_{rel} is calculated for each individual region. The final $D_{\mathrm{rel}}(T)$ then reflects the proportional contribution of each region. A positive $D_{\mathrm{rel}}(T)$ corresponds to a strengthening of the axial dipole moment at the end of the cycle, whilst a negative $D_{\mathrm{rel}}(T)$ corresponds to a weakening.

Note that most SFT simulations, including Jiang et al. (2015), assume that all regions are BMRs with a simple bipolar structure. However in our 2D model this is not always the case. The model inserts the observed shapes of active regions, meaning that complex multipolar configurations are often assimilated. Figure 2 shows

Table 1. Optimal parameter set for the simulation shown in Figure 1. Upper and lower bounds for acceptable parameter ranges are given in square brackets below each entry.

η ($\mathrm{km^2\,s^{-1}}$)	v_0 ($\mathrm{m\,s^{-1}}$)	p	τ (yr)	B_0 (G)
466.8	9.2	2.33	10.1	6.7
[325.7, 747.3]	[5.6, 11.9]	[1.12, 3.95]	[3.6, 31.9]	[0.0, 15.0]

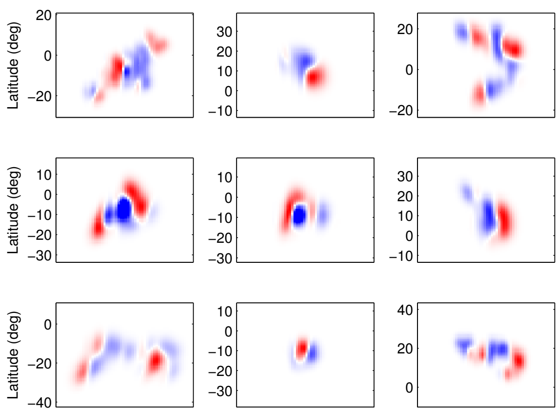

Figure 2. Nine most significant contributing regions from Cycle 23, as measured by $D_{\mathrm{rel}}\,(T)$. The panels are equal in size and centred around each region. Each image is saturated individually.

the configurations of the top nine largest contributors from Cycle 23, as measured by $D_{\mathrm{rel}}\,(T)$. Whilst some regions are clearly bipolar, some are less clear and are harder to separate into BMRs even manually, let alone using an automated algorithm. Because of this, a 'tilt angle' is no longer a sensible measure, and so instead we opt to use the initial (relative) axial dipole moment which still takes into account orientation and polarity. Similarly, we also do not consider polarity separation distance. Another consequence of this is that the model considers a cluster of active regions to be one single large region, whilst human observers would usually separate a sunspot group into multiple BMRs. Hence, for the optimal threshold B_{par}, we tend to extract fewer regions per cycle than other studies. Despite this, the insertion of actual configurations of active regions combined with the optimization procedure means that the overall evolution of the observed axial dipole moment D_{tot} is well reproduced by the simulation, as shown in Figure 11 of Whitbread et al. (2017), even though the axial dipole moment is not considered directly in the fitness function (unlike Lemerle et al. (2015)). We will also continue to use the term 'regions' to describe both individual and clusters of regions.

2.1. *Location and size*

Initially we consider the effects of emergence latitude, flux and initial D_{rel} on the axial dipole moment contribution $D_{\mathrm{rel}}\,(T)$ of each region. The top panels of Figure 3 show the relationships between $D_{\mathrm{rel}}\,(T)$ and these three quantities respectively for the regions from Cycle 21 (1st May 1976–10th March 1986). We find that most significant contributors to the axial dipole moment emerge below ±20°, the very largest of which emerge below ±10°. We also find that these regions do not necessarily have strong levels of magnetic flux; very few of the biggest contributors are stronger than 1.5×10^{22} Mx.

Furthermore, we find that the relationship between initial and final D_{rel} is largely determined by the emergence latitude: regions emerging at mid-latitudes (dark purple) tend to contribute little to the final axial dipole moment, regardless of their initial values. Conversely, regions emerging at low latitudes (yellow and orange) can undergo an increase in axial dipole moment contribution as cross-equatorial flux cancellation occurs and flux is transported poleward by the meridional flow.

The central row of Figure 3 shows the same relationships as discussed above but for Cycle 22 (10th March 1986–1st June 1996). The left and middle panels tell a different story to that of Cycle 21. There are fewer big contributions (i.e. contributions of more than 2.5%) to the axial dipole moment, and the largest is a strengthening rather than a weakening as in Cycle 21. This provides an explanation as to why the axial dipole moment increased in amplitude during Cycle 22. This region is also the only significant contributor to lie below ±10°, although the others still emerge below ±20° as in Cycle 21. The most striking difference between the two cycles is the effect of strong-flux regions. In Cycle 22 some of the most significant contributions to the axial dipole moment come from regions with fluxes above 3×10^{22} Mx, which is not the case in Cycle 21. The same latitudinal dependence of the initial to final D_{rel} relationship is found as in Cycle 21, supporting the idea that latitude of emergence plays an important role in determining whether a region will contribute significantly to the polar field.

The bottom three panels of Figure 3 show the same three distributions but for Cycle 23 (1st June 1996–3rd

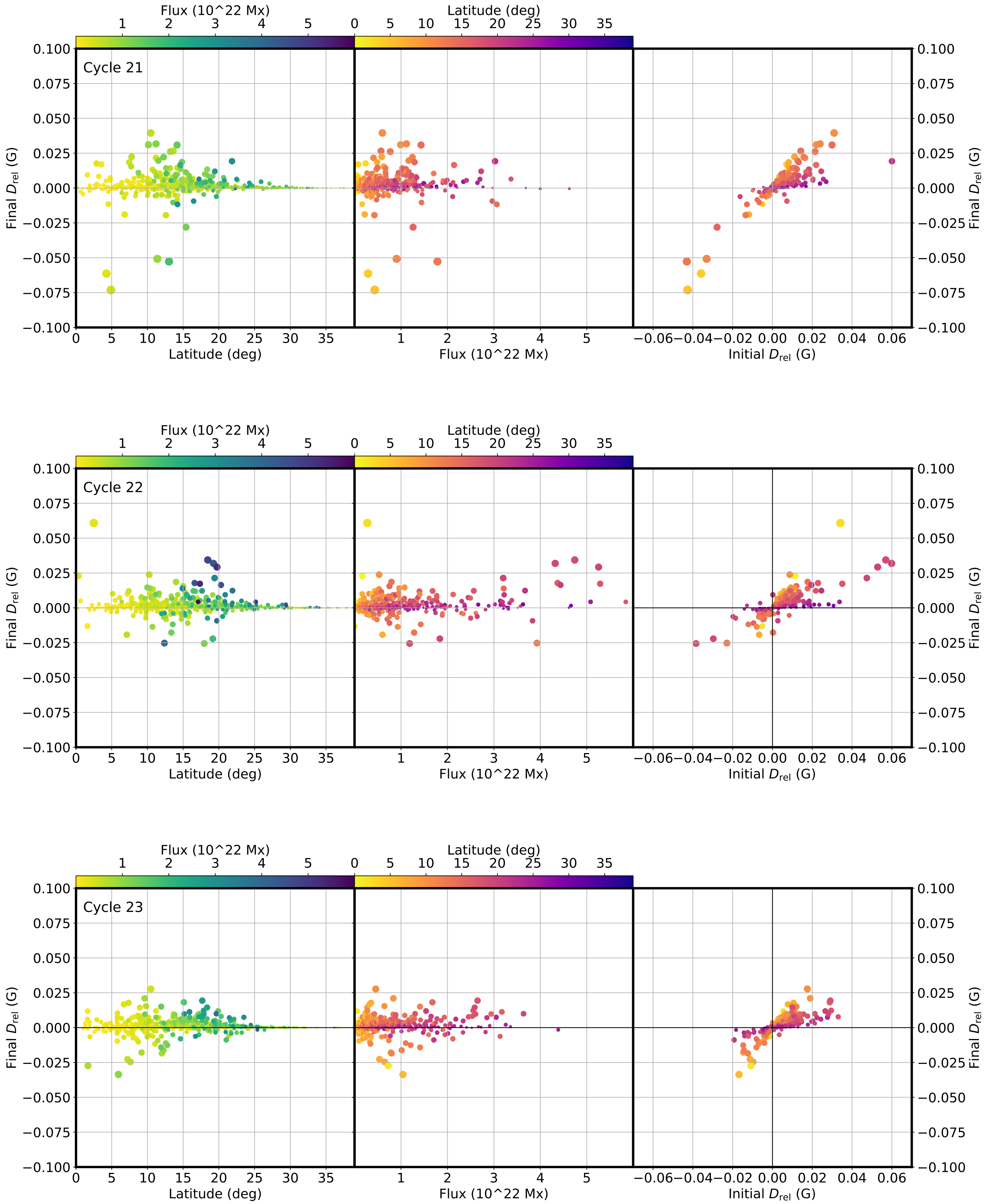

Figure 3. Final $D_{\rm rel}$ for each region against absolute latitude (left panels), flux (middle panels) and initial $D_{\rm rel}$ (right panels). Markers are sized by absolute final $D_{\rm rel}$, and coloured by flux (left panels) and absolute latitude (middle and right panels).

August 2008). We return to a similar regime to Cycle 21: of the most significant contributors, we observe more regions which weaken the axial dipole moment, and the biggest contributors have fluxes smaller than 2×10^{22} Mx. Again, most of these regions emerge below $\pm 20°$. If we consider the sign, we find that the most significant regions in Cycle 23 induce a weakening of the overall axial dipole moment. These low-latitude regions could indeed be the cause of the weak polar field at the end of Cycle 23, and hence the low amplitude of Cycle 24, as suggested by Jiang et al. (2015).

The latitude-dependent relationship between initial and final $D_{\rm rel}$ still holds in Cycle 23. In fact, we can separate the regions into bins of 5° and calculate the gradient of the lines in the right-hand panels of Figure 3 for each bin. We then see in Figure 4 that down to $\pm 20°$ the relationship between initial and final $D_{\rm rel}$ is practically identical across the three cycles, and even down to $\pm 5°$ the relationships over the three cycles are close. For the 0–5° bin, the gradient is much steeper for Cycle 23. However, this bin has relatively few points, and is least well fitted by a linear relationship between initial and final $D_{\rm rel}$, and so we do not consider this to be significant. What should be noted is that the standard errors for these fits are very small, indicating that there is clearly a strong relationship between the overall amplification in $D_{\rm rel}$ and the latitude of emergence. ***If we fit a Gaussian to the data (blue ***same blue as 100 regions profile?*** curve in Figure 4), we find that the axial dipole moment contribution is proportional to $\exp\left(-\frac{\lambda^2}{252}\right)$. This is similar to the relationship between latitude and axial dipole moment contribution in Equation 1.1 given by Jiang et al. (2014) and confirms the Gaussian latitudinal dependence.***

2.2. *Number of regions required*

We now turn to analyse the effect on the overall axial dipole moment of removing small contributions. Regions are listed in order of absolute $D_{\rm rel}\,(T)$ and only those above a certain threshold are assimilated. This routine is performed at five thresholds so that the top 10, 100, 250, 500 and 750 regions are included over five separate runs in each cycle, and the resulting profiles are shown in Figure 5. These are superimposed on the observed axial dipole moment (light grey) to highlight how effectively the optimization of Whitbread et al. (2017) can replicate the observations, despite the axial dipole moment not being directly included in the fitness function for the optimization.

The left-hand section of Figure 5 shows the effect of removing the smallest contributions to the axial dipole moment from the simulation of Cycle 21. Incorporating the largest 750 contributors of the 844 regions makes only a little difference (a decrease of 1.6%), but using 500 regions corresponds to a reduction of 7% of the axial dipole moment.

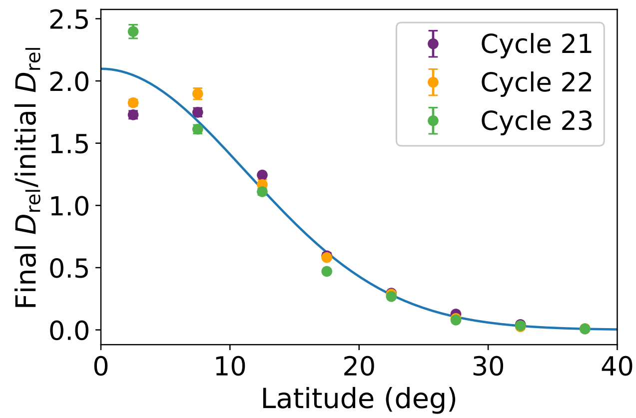

Figure 4. Ratio between final $D_{\rm rel}$ and initial $D_{\rm rel}$ for 5° latitudinal bins for Cycles 21 (purple), 22 (orange) and 23 (green). Error bars show standard error. Markers are plotted at the midpoint of each 5° bin. The blue line is a Gaussian fit to the data.

The middle section of Figure 5 shows the effect of removing the smallest contributions to the axial dipole moment from the simulation of Cycle 22. Again, the effect of removing small contributions is not strong here; as few as 500 of the 846 regions can be used with a shortfall of just 1.3%. Using 750 regions makes very little difference to the evolution of the axial dipole moment. If we assimilate the top ten contributors of Cycle 22, polar field reversal is almost achieved, owing to the fact that the strongest contributors predominantly add to the axial dipole moment, as seen in Section 2.1.

The right-hand section of Figure 5 shows the same profiles as the left and middle sections but for Cycle 23. Even when the largest 750 contributors of the 951 regions are assimilated, there is a more significant discrepancy (a decrease of 4.7%) between the resulting axial dipole moment and the axial dipole moment obtained using every region than in the previous two cycles. Partly this is because the largest contributors in Cycle 23 are less ‘extreme’ than in the previous cycles (as is evident in Figure 3). But it is also compounded by the fact that most of the large contributors in Cycle 23 act to weaken the overall dipole moment (opposite to the majority pattern). The cumulative contribution of many weaker regions is therefore needed to build up its final strength. So although a small number of regions have a disproportionate effect, the cumulative contribution of the many regions with weaker dipole moment cannot be ignored.

In each cycle we see that the top ∼10% of contributors (that is, 1about 100 of them) determine the rapid short-term changes in the axial dipole moment. Here we clearly see the deficit in Cycle 23; even when the top 100 contributors are included the polar field is still unable to reverse. This demonstrates the impact of the strong regions with negative dipole contribution in Cycle 23.

It is imperative to note that there are more total regions involved in our simulations of Cycle 23 than in Cycles 21 and 22, because it is a weaker and therefore longer cycle. The consequence of this is that the same number of regions in Cycle 23 represents a smaller proportion of the total number of regions compared to the other two cycles, and so naturally we might expect the axial dipole moment to be weaker when using, say, 750 regions in Cycle 23. However, when we add more regions to Cycle 23 to balance the proportion with other cycles, there is still a larger difference between the profile with all regions and the profile with some regions removed. We conclude that ultimately this pattern comes down to the polarity distribution of regions with a small contribution to the axial dipole moment, and that the smallest 100 contributors of Cycle 23 must have predominantly positive D_{rel}.

2.3. *Location and time*

We now focus on the time-latitude distributions, i.e. 'butterfly diagrams', of the active regions drawn from the assimilative 2D model. Figure 6 shows the butterfly diagrams of Cycle 21 for the cases shown in the first section of Figure 5, where border colours match profile colours. We find few strong regions that have emerged across the equator, but from Figure 3 we see that there are a couple of regions with strong initial D_{rel}, suggesting that large contributors from Cycle 21 are likely to be because of orientation reasons rather than being cross-equatorial. There is a cluster of negatively contributing regions in the northern hemisphere around 1983 which is not followed by many significant regions during the remainder of the cycle; this cluster could be responsible for a lower axial dipole moment in Cycle 21 (compared to Cycle 22), and explains why the polar field fails to reverse when only 10 regions are used in Cycle 21, as seen in Figure 5.

Figure 7 shows the corresponding butterfly diagrams for Cycle 22. As inferred from Figure 3, the majority of large contributions to the axial dipole moment in Cycle 22 enhance the dipole moment and are clustered around -20°. However, there are two large contributors at low latitudes, possibly cross-equatorial, which would support the claim of Cameron et al. (2013): that regions emerging across the equator can significantly change the amount of net flux in each hemisphere, in turn weakening or strengthening the axial dipole moment, meaning future cycle predictions will be less reliable.

Figure 8 shows the butterfly diagrams of Cycle 23. Significant negatively-contributing regions include a cluster across the equator around 2002, and a group of regions in the southern hemisphere towards the end of the cycle, visible as blue patches in all but the bottom-right frame. While the cross-equatorial group is important for reasons discussed above, the majority of regions in the late-emerging cluster might not have as significant an effect on the current cycle as if they had instead emerged earlier in the cycle, as discussed by Nagy et al. (2017). Nevertheless, by analysing Cycles 21 and 23 we see that a lack of disruption from a major cross-equatorial region in Cycle 21 led to a stronger axial dipole moment compared to Cycle 23. The butterfly diagrams have also confirmed that the largest contributors are not necessarily the biggest in terms of flux.

2.4. *Effect of decay on the axial dipole moment*

As mentioned in Section 2, we also remove the decay term from Equation 2.1 and repeat the optimization and subsequent analysis on the same three cycles. Whilst the equivalent distributions as those shown in the scatterplots of Section 2.1 and butterfly diagrams of Section 2.3 are qualitatively indistinguishable up to a scaling factor, the axial dipole moment profiles with regions removed as shown in Section 2.2 behave slightly differently, simply because of the lack of decay impacting on cycle minima. The profiles from simulations without decay are shown in Figure 9. With less freedom from fewer parameters, the optimal axial dipole moment does not match the observed counterpart as well when decay is included, but the fit is still acceptable.

Again we find that when the top 750 contributors are used, Cycles 21 and 22 are hardly affected but the discrepancy in Cycle 23 is now even more visible than before. When the 100 largest contributors are used, the polar field reverses in Cycles 21 and 22, but not in Cycle 23. Furthermore, polar field reversal is only just achieved with 250 regions, supporting the claim that the biggest contributors from Cycle 23 contribute negatively to the axial dipole moment. For Cycle 21, Wang & Sheeley (1991) found that about 54% of the axial dipole moment came from about 10.7% of regions, and here we find a similar result (blue curve). In fact, we find the same outcome for Cycle 22 but not for Cycle 23.

3. ***WHAT ARE THE IMPLICATIONS FOR MAKING PREDICTIONS?***

Up to this point regions have been ordered by final D_{rel}. Unfortunately, calculating this at time of emer-

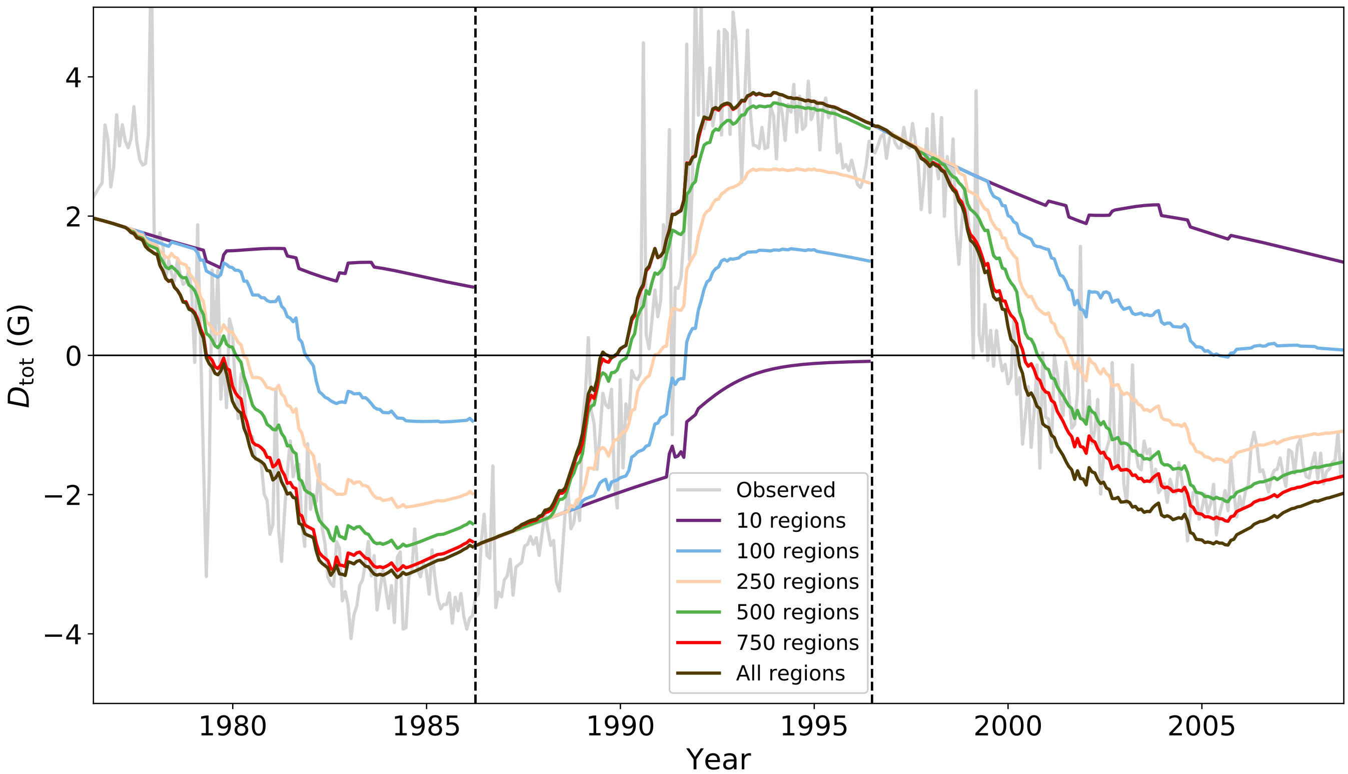

Figure 5. Evolution of the axial dipole moment for Cycles 21 to 23. Each profile is obtained by only using a certain number of the biggest contributors to the axial dipole moment. The legend shows the number of regions from each cycle per profile. The light grey curve shows the observed axial dipole moment. Vertical dashed lines indicate start/end points of cycles as used in this paper.

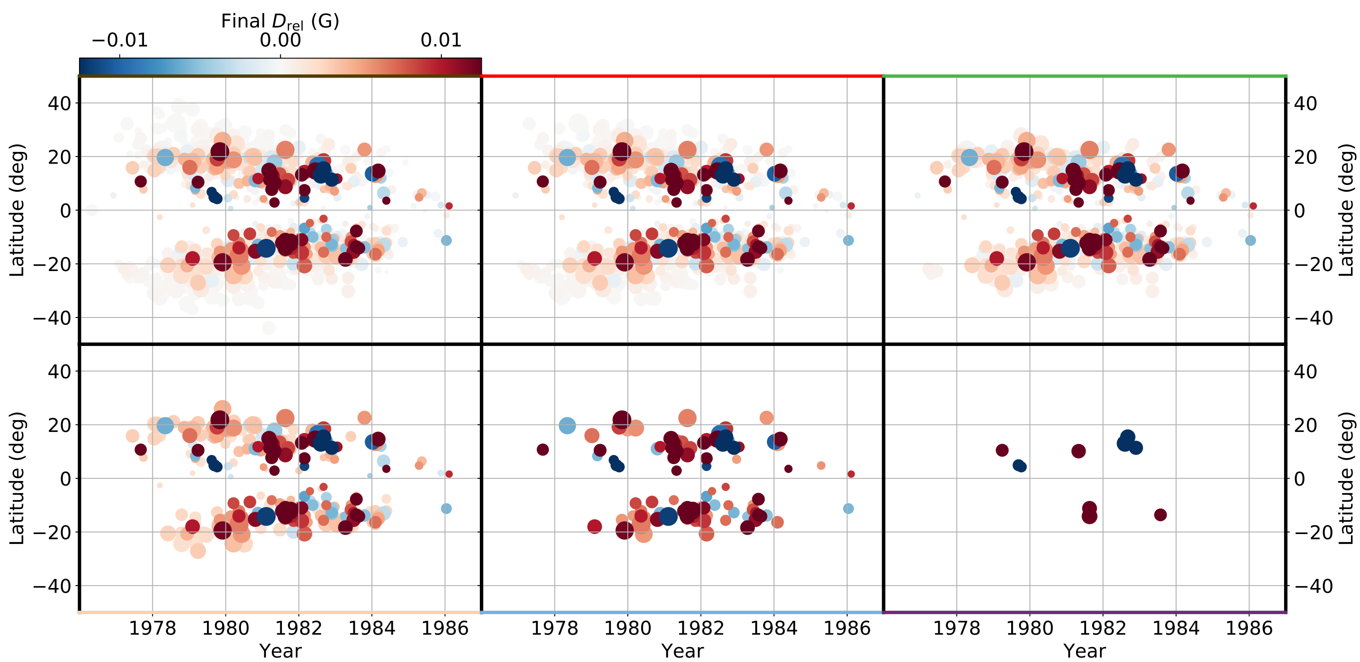

Figure 6. Time-latitude distributions of regions from Cycle 21 used to obtain the profiles in the first section of Figure 5 (profile colours match border colours). Markers are sized by flux and coloured by final D_{rel}.

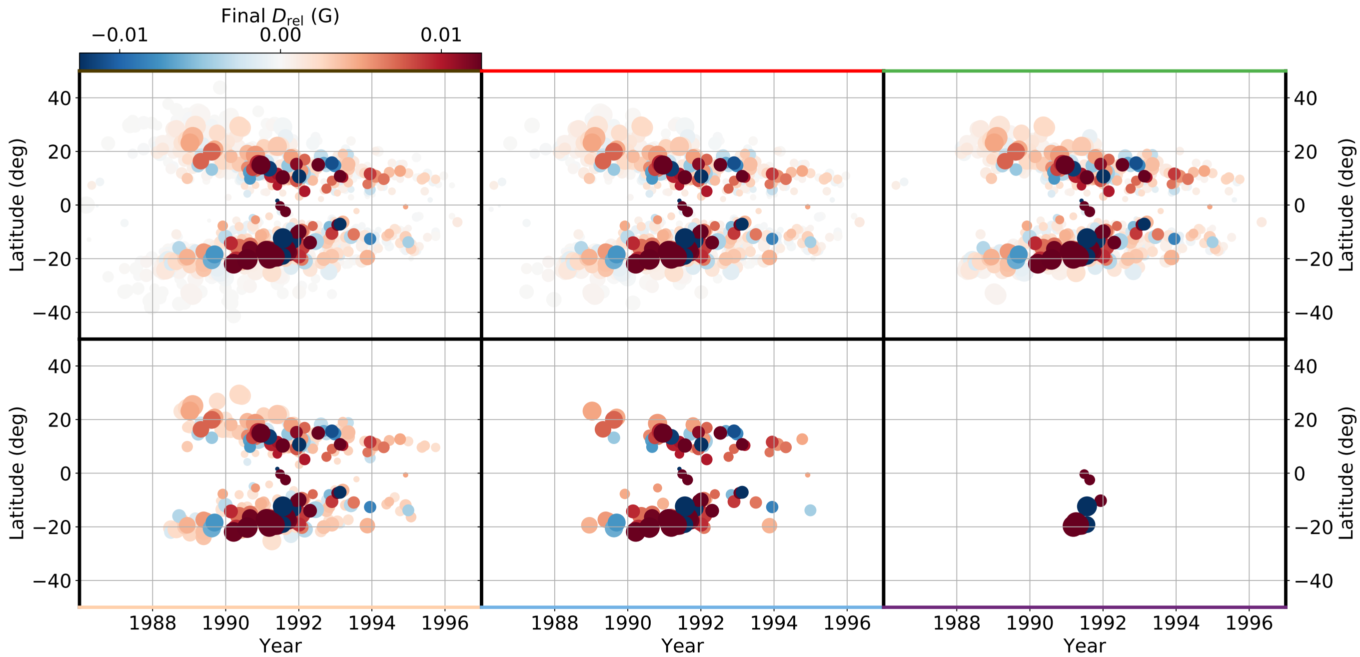

Figure 7. Time-latitude distributions of regions from Cycle 22 used to obtain the profiles in the second section of Figure 5 (profile colours match border colours). Markers are sized by flux and coloured by final $D_{\rm rel}$.

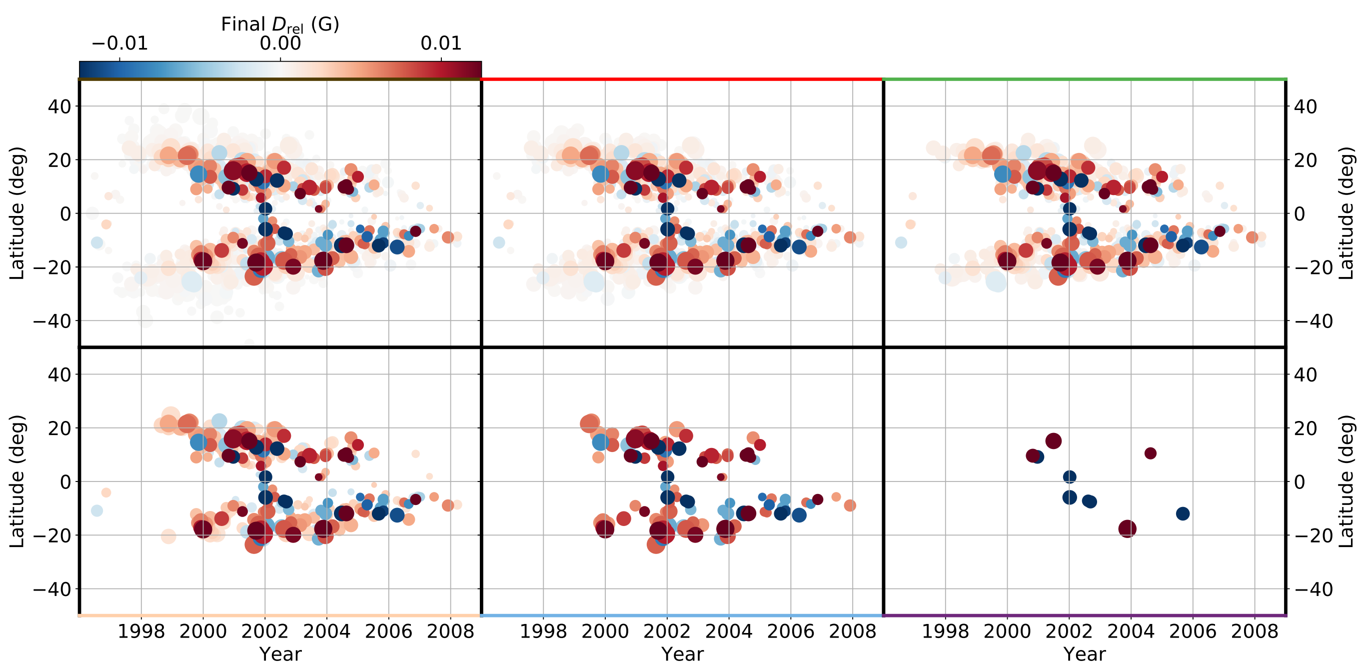

Figure 8. Time-latitude distributions of regions from Cycle 23 used to obtain the profiles in the third section of Figure 5 (profile colours match border colours). Markers are sized by flux and coloured by final $D_{\rm rel}$.

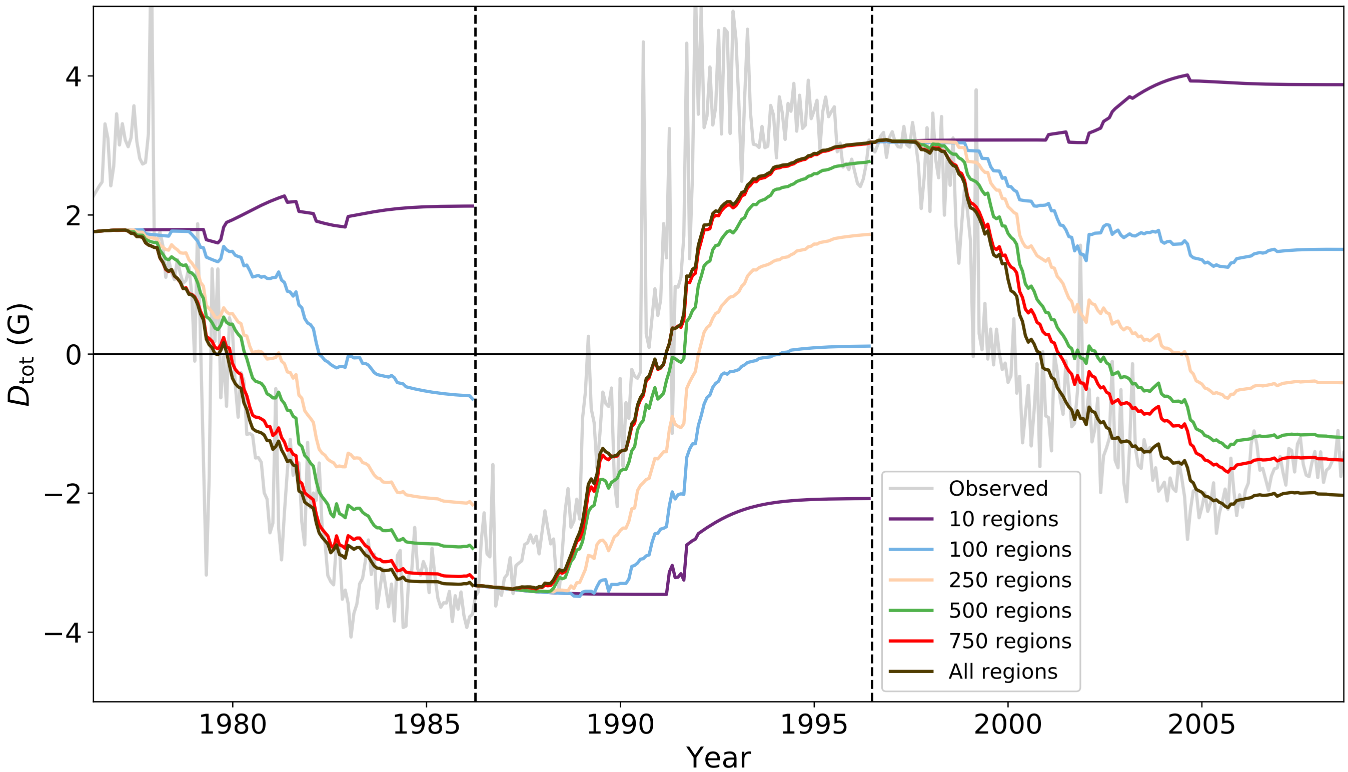

Figure 9. Evolution of the axial dipole moment for Cycles 21 to 23 with no exponential decay term. Each profile is obtained by only using a certain number of the biggest contributors to the axial dipole moment. The legend shows the number of regions from each cycle per profile. The light grey curve shows the observed axial dipole moment. Vertical dashed lines indicate start/end points of cycles as used in this paper.

gence requires us to know the subsequent behaviour during the rest of the cycle. It is possible to estimate from an empirical formula such as Equation 1.1, but the relationship between initial state and $D_{\rm rel}$ is not exactly the same for all regions across all cycles, as shown in Figure 4, and any calculation made is only an estimation with an accompanying error. Instead we examine the consequences of ordering and excluding regions based on absolute flux, which is a quantity readily measured at time of observation. Figure 10 displays the change in $D_{\rm rel}$ as more active regions are included in the simulation, ordered by decreasing flux, for Cycles 21 (green), 22 (orange) and 23 (purple). This further highlights the distinctions between the three cycles.

There are multiple regions with large flux that contribute positively to the axial dipole moment during Cycle 21. Because of this, 80% of the axial dipole moment is attained when less than 40% of regions are considered (bearing in mind the threshold for the top 40% is $\sim$4–4.5×10^{21} Mx depending on the cycle). There is then a sharp decrease when the two biggest contributions are included, before the 80% mark is reached again, corresponding to half the number of regions being used. Note that more than 25% of the axial dipole moment is attained by the single largest region alone. This is the effect of exponential decay, which decreases the axial dipole moment contribution of a small number of regions so that it is closer to $D_{\rm tot}\,(T)$ at the end of a cycle (see Figure 5 and compare with Figure 9). This effect is even stronger for the other two cycles.

The $D_{\rm rel}$ of Cycle 22 rises at a steady rate as more regions are added, but there are two clear phases with a large jump in between. One can attribute this jump to the inclusion of the largest contributor of Cycle 22, which is weak in terms of flux (see Figure 3). Because of this significant addition to the dipole moment, using 55% of regions is enough to ensure that 80% of the axial dipole moment is reached.

The profile for Cycle 23 initially reaches almost $0.5\,D_{\rm rel}$, presumably because the strongest regions contribute positively to the dipole moment as we see in Figure 3. There is then barely an increase in final $D_{\rm rel}$ as another 30% of the regions are included. This mimics the problem found in Figure 5; Cycle 23 is largely dominated by negative $D_{\rm rel}$ active regions.

We hope this will give insight to those wishing to model full solar cycles, in particular giving an indication as to what resolution is sufficient (or equivalently how

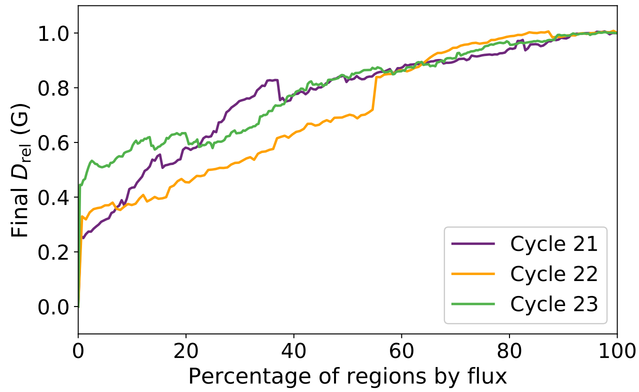

Figure 10. $D_{\rm rel}$ against percentage of regions included for Cycles 21 (purple), 22 (yellow) and 23 (green). Regions are ordered by flux and the top x% of the strongest regions are incorporated.

small regions are allowed to be in order to be ignored), to give an acceptable representation of the axial dipole moment. It may be noteworthy that when 60% of the strongest regions are incorporated (i.e. regions with flux above about 2×10^{21} Mx), the three cycles reach 80% of the final $D_{\rm rel}$ and adding small regions bears minimal difference, regardless of cycle number. If 90% of regions are used, corresponding to a strength of approximately 5×10^{20} Mx and above, all three cycles reach a similar relative level close to $D_{\rm tot}\,(T)$.

4. CONCLUSIONS

Our aim was to extract active region properties from magnetograms using an automated region assimilation technique, and analyse the relationships between these properties and the evolution of the axial dipole moment using a 2D flux transport model. We examined how the final contribution of a single region to the axial dipole moment at the end of the cycle is affected by a region's latitude, flux and initial axial dipole moment, and compared these relationships across Cycle 21, 22 and 23.

We found some consistent results across all three cycles. Generally all large contributions to the axial dipole moment emerge below $\pm 20°$, with the largest emerging below $\pm 10°$. This supports the idea that regions emerging at low-latitude can have a large effect on the evolution of the axial dipole moment (Cameron et al. 2013; Jiang et al. 2015). However, this previous work also combined the latitudinal dependence with the effect of random scatter of tilt angles. For our more realistically shaped multipolar regions, we cannot measure the conventional tilt angle, so instead we calculated the more meaningful parameter of initial $D_{\rm rel}$ which takes into account orientation as well as latitude. We found a general positive correlation between initial and final $D_{\rm rel}$ within all latitudinal bins in all cycles, but that the constant of proportionality depended on latitude with regions at low latitudes contributing most, whence we conclude that emergence latitude is the dominant parameter controlling the amplification or suppression of the initial dipole moment of a region.

We found that the patterns of regions contributing most to the dipole moment were not consistent across the three cycles. In particular, Cycle 22 contained multiple strong-flux regions which were also some of the largest contributors to the axial dipole moment. This was not the case in Cycles 21 and 23; most large contributors had fluxes of less than 2×10^{22} Mx, reinforcing that flux alone is not an appropriate measure of contribution. We conclude that while emergence latitude appears to be the most important property in determining a region's contribution to the axial dipole moment, there is also an important dependence on size and tilt/orientation. This reinforces the expression of the kind given in Equation 1.1. Nagy et al. (2017) showed that changing BMR tilt and emergence latitude had more immediate consequences than changing flux, unless a very large amount of flux was included. Consequently, if a very large, anti-Joy, anti-Hale region was to emerge close to the equator, it could have a significant detrimental impact on the polar field and hence the amplitude of the next cycle. Following the results of Nagy et al. (2017) it could even be speculated that, in the most extreme case, such an event could lead to a grand minimum.

We also looked at the effect of removing regions with the smallest final $D_{\rm rel}$ in increments. Using the 500 biggest contributors produced an acceptable axial dipole moment in Cycles 21 and 22, but the removal was more damaging in Cycle 23, where at least 750 regions are required to produce an acceptable match. Similarly, when regions are removed in order of flux, there are differences between cycles; different percentages of regions are needed to achieve acceptable matches in different cycles.

As we approach the minimum at the end of Cycle 24, predictions of Cycle 25 will become more reliable, since it becomes less likely that any more large regions which can significantly alter the polar field will emerge. Indeed, from our analysis of the previous three cycles, we only found significant contributors emerging up to the early stages of the descending phase, although that isn't to say such an event is not possible. Indeed, Nagy et al. (2017) found that 'rogue' regions emerging late in the cycle can still have an effect on the following cycle, but this cannot be assessed using our surface flux transport approach, and requires simulation of the interior of the convection zone. For completeness we should go back and repeat this analysis once we reach cycle minimum in a few years' time, using the results to assess any current predictions of Cycle 25.

Some predictions of Cycle 25 have already been made, for example by Hathaway & Upton (2016) and Cameron et al. (2016), who used two distinct models but came to a similar conclusion: that Cycle 25 will be another weak cycle. However, by incorporating uncertainty in tilt angles and performing multiple simulations, a wider range of cycle amplitudes was found, suggesting that the behaviour of our Sun really does hinge on the random fluctuations in active region properties, and perhaps making *early* predictions of the next cycle, let alone future cycles, is futile.

TW thanks Durham University Department of Mathematical Sciences for funding his PhD studentship. ARY thanks STFC for financial support. We thank Gordon Petrie for supplying the data in Figure 1, and magnetogram data were acquired by SOLIS instruments operated by NISP/NSO/AURA/NSF. This work was partly funded by NASA Grand Challenge grant NNH13ZDA001N. ***AMJ?***

REFERENCES

Babcock, H. W. 1961, ApJ, 133, 572, doi: 10.1086/147060

Baumann, I., Schmitt, D., & Schüssler, M. 2006, A&A, 446, 307, doi: 10.1051/0004-6361:20053488

Baumann, I., Schmitt, D., Schüssler, M., & Solanki, S. K. 2004, A&A, 426, 1075, doi: 10.1051/0004-6361:20048024

Cameron, R. H., Dasi-Espuig, M., Jiang, J., et al. 2013, A&A, 557, A141, doi: 10.1051/0004-6361/201321981

Cameron, R. H., Jiang, J., & Schüssler, M. 2016, ApJL, 823, L22, doi: 10.3847/2041-8205/823/2/L22

Cameron, R. H., Jiang, J., Schüssler, M., & Gizon, L. 2014, Journal of Geophysical Research (Space Physics), 119, 680, doi: 10.1002/2013JA019498

Charbonneau, P. 2014, ARA&A, 52, 251, doi: 10.1146/annurev-astro-081913-040012

Charbonneau, P., & Knapp, B. 1995, NCAR Tech. Note, NCAR/TN-418+IA (Boulder, CO: National Center for Atmospheric Research), 1

Fan, Y. 2009, Living Reviews in Solar Physics, 6, doi: 10.12942/lrsp-2009-4

Hale, G. E. 1924, Proceedings of the National Academy of Science, 10, 53, doi: 10.1073/pnas.10.1.53

Hathaway, D. H., & Upton, L. A. 2016, Journal of Geophysical Research (Space Physics), 121, 10, doi: 10.1002/2016JA023190

Howard, R. 1979, ApJL, 228, L45, doi: 10.1086/182900

Howard, R. F. 1991, SoPh, 136, 251, doi: 10.1007/BF00146534

Jackiewicz, J., Serebryanskiy, A., & Kholikov, S. 2015, ApJ, 805, 133, doi: 10.1088/0004-637X/805/2/133

Jiang, J., Cameron, R. H., & Schüssler, M. 2014, ApJ, 791, 5, doi: 10.1088/0004-637X/791/1/5

—. 2015, ApJL, 808, L28, doi: 10.1088/2041-8205/808/1/L28

Jiang, J., Işik, E., Cameron, R. H., Schmitt, D., & Schüssler, M. 2010, ApJ, 717, 597, doi: 10.1088/0004-637X/717/1/597

Komm, R. W., Howard, R. F., & Harvey, J. W. 1993, SoPh, 147, 207, doi: 10.1007/BF00690713

Leighton, R. B. 1964, ApJ, 140, 1547, doi: 10.1086/148058

Lemerle, A., Charbonneau, P., & Carignan-Dugas, A. 2015, ApJ, 810, 78, doi: 10.1088/0004-637X/810/1/78

Li, J., & Ulrich, R. K. 2012, ApJ, 758, 115, doi: 10.1088/0004-637X/758/2/115

Mackay, D. H., & Yeates, A. R. 2012, Living Reviews in Solar Physics, 9, 6, doi: 10.12942/lrsp-2012-6

Metcalfe, T. S., & Charbonneau, P. 2003, Journal of Computational Physics, 185, 176, doi: 10.1016/S0021-9991(02)00053-0

Muñoz-Jaramillo, A., Dasi-Espuig, M., Balmaceda, L. A., & DeLuca, E. E. 2013, ApJL, 767, L25, doi: 10.1088/2041-8205/767/2/L25

Muñoz-Jaramillo, A., Sheeley, N. R., Zhang, J., & DeLuca, E. E. 2012, ApJ, 753, 146, doi: 10.1088/0004-637X/753/2/146

Nagy, M., Lemerle, A., Labonville, F., Petrovay, K., & Charbonneau, P. 2017, SoPh, 292, 167, doi: 10.1007/s11207-017-1194-0

Petrie, G. J. D. 2012, SoPh, 281, 577, doi: 10.1007/s11207-012-0117-3

Schatten, K. H., Scherrer, P. H., Svalgaard, L., & Wilcox, J. M. 1978, Geophys. Res. Lett., 5, 411, doi: 10.1029/GL005i005p00411

Schrijver, C. J., De Rosa, M. L., & Title, A. M. 2002, ApJ, 577, 1006, doi: 10.1086/342247

Sheeley, Jr., N. R. 2005, Living Reviews in Solar Physics, 2, 5, doi: 10.12942/lrsp-2005-5

Snodgrass, H. B., & Ulrich, R. K. 1990, ApJ, 351, 309, doi: 10.1086/168467

Stenflo, J. O., & Kosovichev, A. G. 2012, ApJ, 745, 129, doi: 10.1088/0004-637X/745/2/129

Svalgaard, L., Duvall, Jr., T. L., & Scherrer, P. H. 1978, SoPh, 58, 225, doi: 10.1007/BF00157268

Upton, L., & Hathaway, D. H. 2014, ApJ, 780, 5, doi: 10.1088/0004-637X/780/1/5

Wang, Y.-M., Nash, A. G., & Sheeley, Jr., N. R. 1989, ApJ, 347, 529, doi: 10.1086/168143

Wang, Y.-M., & Sheeley, Jr., N. R. 1991, ApJ, 375, 761, doi: 10.1086/170240

Whitbread, T., Yeates, A. R., Muñoz-Jaramillo, A., & Petrie, G. J. D. 2017, A&A, 607, A76, doi: 10.1051/0004-6361/201730689

Yeates, A. R., Baker, D., & van Driel-Gesztelyi, L. 2015, SoPh, 290, 3189, doi: 10.1007/s11207-015-0660-9